

# Star Formation Triggered by the expanding bubble S111

BHASWATI MOOKERJEA<sup>1</sup>

<sup>1</sup>*Tata Institute of Fundamental Research,  
Homi Bhabha Road, Mumbai 400005, India*

Submitted to APJ

## ABSTRACT

This paper investigates the impact of radiative and mechanical feedback from O-type stars on their parent molecular clouds and the triggering of formation of future generation of stars. We study the infrared bubble S111 created by the embedded massive stellar cluster G316.80-0.05. A significant fraction of gas in shells created due to the compression of the ambient medium by expanding bubbles is photodissociated by the stellar radiation. The kinematics of the shells are thus best studied using spectroscopic observations of singly ionized carbon, the most dominant species. We have used the velocity-resolved maps of the  $^2P_{3/2} \rightarrow ^2P_{1/2}$  transition of [C II] at  $158\ \mu\text{m}$ , the  $J=2-1$  transition of  $^{13}\text{CO}$  and  $\text{C}^{18}\text{O}$ , and the  $J=1-0$  transition of  $\text{HCO}^+$  to study the rim of the bubble S111 that partly coincides with the southern part of the infrared dark ridge G316.75. The [C II] spectra conclusively show evidence of a shell expanding with a moderate velocity of  $\sim 7\ \text{km s}^{-1}$ , which amounts to a kinetic energy that is  $\sim 0.5-40$  times the thermal energy of the H II region. The pressure causing the expansion of the H II region arises mainly from the hydrogen ionization and the dust-processed radiation. Among the far-infrared sources located in the compressed shells, we find the core G316.7799-0.0942 to show broad spectral features consistent with outflow activity and conclude that it is a site of active star formation. Based on the age of the H II region we conclude that this expanding H II region is responsible for the triggering of the current star formation activity in the region.

**Keywords:** ISM: Bubbles – infrared: ISM – ISM: lines and bands –(ISM:) photon-dominated region (PDR) –ISM: individual (S111) –ISM: individual (G316.75) – ISM: kinematics and dynamics

## 1. INTRODUCTION

Massive stars play a dominant role in the injection of UV radiation into the interstellar medium (ISM) and of mechanical energy through stellar winds and finally through supernova explosions. The photoionization, radiation pressure, and stellar winds from young O-type stars pump both energy and momentum into the ambient material and disrupt the parent molecular cloud by creating H II regions and parsec-size bubbles enclosed by shells of denser swept-up material (Churchwell et al. 2006, and references therein). It is envisaged that such radiative and mechanical feedback from the massive stars regulate the star forming

environment locally as well as influence the evolution of the ISM in the galaxies as a whole (Krumholz et al. 2018). Inventories of such bubbles have been primarily derived from large-scale mid-infrared continuum images observed using the Spitzer and AKARI telescopes (Deharveng et al. 2010; Hanaoka et al. 2020).

The triple bubble system consisting of S109, S110, and S111 (Churchwell et al. 2006) is created by the bipolar ionized nebula G316.80-00.05 oriented approximately northeast to southwest as well as an older outflow extending to the east (Dalglish et al. 2018). The parent molecular cloud in this region is primarily in the form of a ridge that hosts the embedded massive stellar cluster associated with the H II region. The ridge is seen in absorption in the visible, near-infrared, and at Spitzer-GLIMPSE wavelengths (Fig. B.1a in Samal et al. 2018), and is clearly detected in emission at the Herschel-SPIRE wavelengths and in the 870  $\mu\text{m}$  ATLASGAL images. In this system the S110 bubble is the northern lobe, which extends perpendicular to the filament, while S109 and S111 form the southern lobe (Fig. 1). The complex morphology of the region is attributed to the inhomogeneous density distribution that causes the ionization front to be distorted and enables leakage of ionizing photons to large distances from the embedded cluster as evidenced by the presence of diffuse emission from the ionized gas in S110 and S111 (Samal et al. 2018). The dust temperature distribution derived from the Herschel Hi-GAL (Molinari et al. 2010) continuum observations suggests that while the parental filament is cold ( $\sim 17$  K), going down to 14 K, the photon dominated regions (PDRs) register temperatures well above 20 K (Samal et al. 2018). The column density at the position of peak temperature position is  $\sim 10^{23} \text{ cm}^{-2}$ , which corresponds to a visual extinction of  $\sim 100$  mag, which explains why the stellar cluster ionizing the region is not detected in the visible and near-IR.

In this paper, we refer to the ridge as G316.75 and the H II region as G316.80-00.05. The G316.75 ridge located at a distance of  $2.69 \pm 0.45$  kpc (Watkins et al. 2019) extends over 13.6 parsec. The southern part of the ridge, which is associated with an infrared dark cloud (SDC316.786-0.044 Peretto & Fuller 2009), is more active than the northern part (Watkins et al. 2019). Shaver et al. (1981) were the first to confirm the near kinematic distance of G316.75 and determined that the source of the H II region to be an O6-type star. Using radiative transfer modeling of near- to far-infrared dust continuum emission, Vig et al. (2007) had estimated that two O-type stars of masses  $45 M_{\odot}$  and  $25 M_{\odot}$  are responsible for most of the infrared luminosity of G316.75. This is also corroborated by high-angular-resolution radio continuum and hydrogen recombination line observations (Longmore et al. 2009) which detected two 24 GHz continuum sources at resolutions better than  $10''$ . Watkins et al. (2019) have subsequently concluded that two high-mass stars with spectral types of O8.5–O7 V and O6.5–O6 V can explain the observed emission from the ionized gas from the region. Dalglish et al. (2018) have studied the kinematics of the ionized gas using radio recombination line (RRL) emission, and concluded that the strong velocity gradient they observe could be a relic of the cloud’s initial angular momentum. Study of the southern part of the ridge G316.75 is rendered interesting by the fact that is a very active and young star-forming region, harboring water, hydroxyl, and methanol masers, several O-stars, and a compact X-ray source, and it is characterized by very dynamic gas conditions.

Beyond the ionized gas, a significant fraction of the neutral (atomic and molecular) material in the vicinity of such embedded clusters in the bubbles is impacted by the far-ultraviolet (FUV:6–13 eV) radiation creating the so-called PDRs. In the far-infrared (FIR) the most important cooling lines from PDRs are the fine structure lines of [C II] at 158  $\mu\text{m}$  and [O I] at 63 and 145  $\mu\text{m}$ , and to a lesser extent, high- $J$  CO lines, while polycyclic aromatic hydrocarbon (PAH) emission and H<sub>2</sub> lines dominate in the near- and mid-IR. The ionization potential of carbon being 11.26 eV, C<sup>+</sup> is expected to exist in ionized, atomic, and molecular gas. As a result [C II] has a unique position as a tracer of PDR gas owing to the ubiquity of carbon and the moderate excitation conditions ( $E_{\text{up}}=92$  K,  $n_{\text{cr}}=3000 \text{ cm}^{-3}$ ) of the transition. Thus, [C II] at 158  $\mu\text{m}$

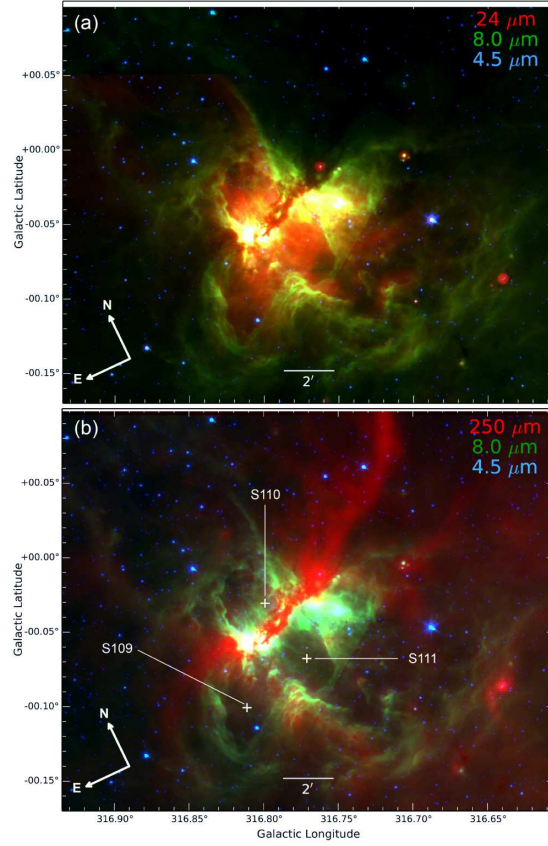


**Figure 1.** Bipolar nebula G316.80-00.05. (a) Composite color image of the G316.790-0.045 complex: red, green, and blue indicate the Spitzer 24, 8.0, and 4.5  $\mu\text{m}$  data, respectively (the 24  $\mu\text{m}$  emission is saturated in the center). (b) Composite color image of the complex: red is for the Herschel 250  $\mu\text{m}$  emission showing the cold filament at the waist of the nebula, green is for the 8  $\mu\text{m}$  PAH emission, and blue is for the 4.5  $\mu\text{m}$  stellar emission. The three bubbles listed in the (Churchwell et al. 2006) catalog are marked. Figure reproduced from Samal et al. (2018) with permission.

is an ideal tool for tomographic study of the morphology and kinematics of photoirradiated bubbles. The availability of far-infrared observing facilities with multi-pixel receivers has recently enabled study of the velocity fields in the Galactic PDRs using the information derived from mapping observations of [C II] at 158  $\mu\text{m}$ .

In this paper we study the morphology and kinematics of the PDR gas in the G316.75 region that is exposed to the FUV radiation from the embedded massive stellar cluster that also gives rise to the bipolar H II nebula G316.8-0.05. For this purpose we primarily use the velocity information derived from observations of [C II] emission at 158  $\mu\text{m}$  in combination with  $^{13}\text{CO}(2-1)$  and  $\text{HCO}^+(1-0)$  emission that arises primarily from the molecular material.

## 2. OBSERVATIONS

The paper makes use of several sets of publicly available data, which are described below.

### 2.1. GREAT/SOFIA observations

We have retrieved observations of the  $^2\text{P}_{3/2} \rightarrow ^2\text{P}_{1/2}$  fine structure transition of ionized carbon ( $\text{C}^+$ ) at 1900.5369 GHz (157.74  $\mu\text{m}$ ) of the region around the G316.8-00.05 from the data archive of the Stratospheric Observatory for Infrared Astronomy (SOFIA; Young et al. 2012). The observations (Id: 06\_0074;

PI: J. Jackson) were carried out using the German REceiver for Astronomy at Terahertz frequencies (GREAT; Heyminck et al. 2012) on 2018 June 22. The beam size for [C II] was  $14''.1$ . The [C II] map extends over a  $500'' \times 600''$  area and observations were carried out in total power on-the-fly mode. We used the Level 4 data available on the SOFIA archive for the region. All data were smoothed to a spectral resolution of  $0.25 \text{ km s}^{-1}$  resulting in an rms of 0.8 K. The [O I]  $63 \mu\text{m}$  fine structure transition was also mapped simultaneously as part of the same project. However, since the mapping was optimized for [C II], the [O I] data were undersampled and smeared in the scan direction and hence were not used in this work.

## 2.2. SEDIGISM

We have used the data cubes for  $J=2-1$  transition of  $^{13}\text{CO}$  and  $\text{C}^{18}\text{O}$  that were observed as a part of the large-scale ( $84 \text{ deg}^2$ ) spectroscopic survey of the inner Galactic disk, named Structure, Excitation and Dynamics of the Inner Galactic Interstellar Medium (SEDIGISM; Schuller et al. 2021). These data were observed with the APEX telescope between 2013 and 2016 with an angular resolution of  $30''$  and a  $1\sigma$  sensitivity less than  $1.0 \text{ K}$  at  $0.25 \text{ km s}^{-1}$  velocity resolution.

## 2.3. MALT90

The Millimetre Astronomy Legacy Team 90 GHz (MALT90) survey (Foster et al. 2011, 2013; Jackson et al. 2013) mapped a sample of high-density cores in 16 transitional lines including the high-density tracer  $\text{HCO}^+(1-0)$  at  $89188.5234 \text{ MHz}$ . These data were taken with the 22 m Mopra radio telescope by individually observing each of the  $\sim 2000$  targeted clumps in a  $3' \times 3'$  data cube. The data cubes have an angular resolution of  $38''$  and an rms noise of  $0.2 \text{ K}$  at a spectral resolution of  $\sim 0.11 \text{ km s}^{-1}$ . Three MALT90 observations lie within the region studied here. We have in particular used the data for  $\text{HCO}^+(1-0)$  with a critical density of  $2 \times 10^5 \text{ cm}^{-3}$  to understand the kinematics of the underlying dense gas in the region.

# 3. IMPACT OF MASSIVE O-STARS IN G316.75 ON THE RIDGE

Watkins et al. (2019) have performed a detailed analysis of the radio continuum emission from the embedded G316.75 stellar cluster that irradiates the ridge and its vicinity. The mass of the stellar cluster is  $930 \pm 230 M_{\odot}$  and it consists of four O-type stars one of which has a mass larger than  $48 M_{\odot}$ . The ionizing stars responsible for the two radio continuum peaks seen in the Sydney University Molongolo Sky Survey (SUMSS Mauch et al. 2003) were further constrained to be due to two high-mass stars with spectral types O8.5–O7 and O6.5–O6. The dynamical age of a G316.75-like H II region with a radius of  $6.5 \text{ pc}$  and a Lyman continuum photon production rate,  $N_{\text{Lyc}} = 10^{49.63} \text{ s}^{-1}$  was estimated to be  $\sim 2 \text{ Myr}$ .

Earlier studies using primarily tracers of ionized and molecular material concluded that the G316.75 ridge is mostly unaffected by ionization owing to the large electron and  $\text{H}_2$  gas densities in the immediate vicinity of the ionizing high-mass stars (Watkins et al. 2019). These authors argued that ionization due to OB stars happened after the formation of the molecular ridge. Here we concentrate on the distribution and velocities of the FUV-irradiated gas as traced by the PDR tracer – the [C II] line at  $158 \mu\text{m}$  – to study the radiative and mechanical feedback of the ionizing stars primarily on the S111 bubble.

## 4. RESULTS

The velocity-integrated [C II] map shows three bright emission regions, one centered on the bright radio continuum emission in the southern part of the ridge, one to the southeast of it, and one to the east, skirting the S111 bubble (Fig. 2). All three emission regions are connected by faint [C II] emission arising from

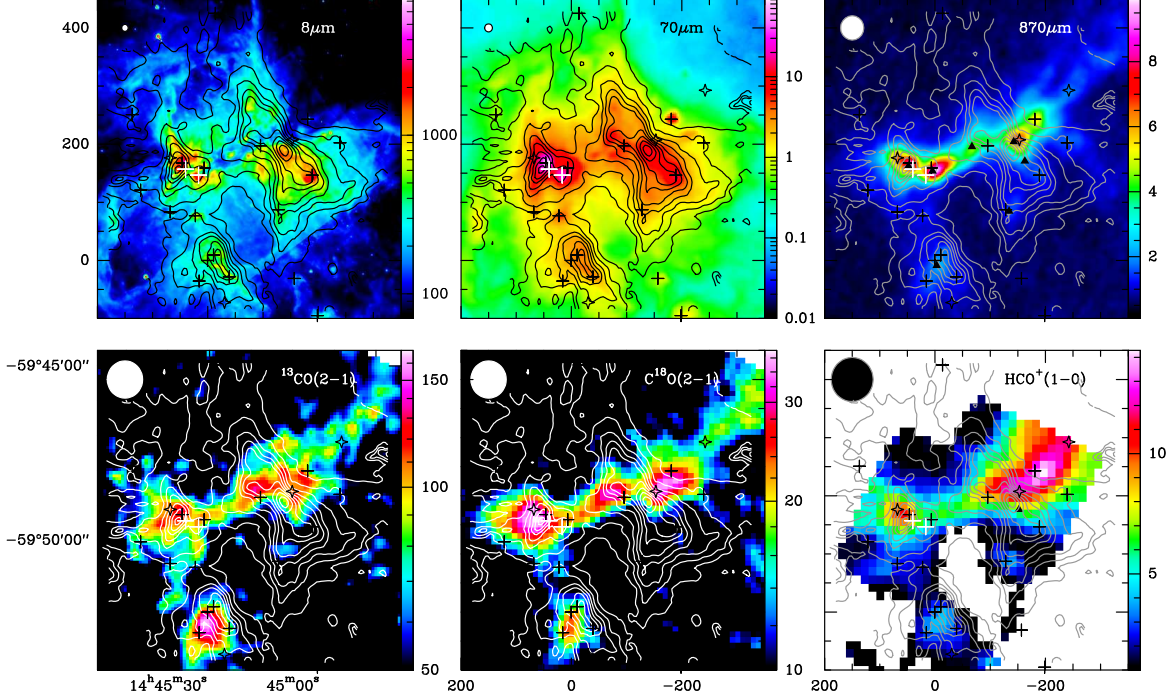


**Figure 2.** Comparison of [C II] emission at  $158\ \mu\text{m}$  emission integrated between  $-65$  and  $-20\ \text{km s}^{-1}$  (contours) with emission due to other tracers of dust, PAHs, and molecular gas (in color and names marked in each panel). The [C II] contours are drawn from  $90$  to  $540\ \text{K km s}^{-1}$  in steps of  $50\ \text{km s}^{-1}$ . The color scale corresponding to each panel is included to the right of it. The units are  $\text{MJy sr}^{-1}$  for the  $8\ \mu\text{m}$  image,  $\text{Jy pixel}^{-1}$  for  $3''$  pixels for the PACS  $70\ \mu\text{m}$  image, and  $\text{Jy beam}^{-1}$  with a beam size of  $21''$  for the ATLASGAL  $870\ \mu\text{m}$ . The color scales of spectroscopic images are all in units of  $\text{K km s}^{-1}$ . The velocity intervals of integration of  $^{13}\text{CO}(2-1)$ ,  $\text{C}^{18}\text{O}(2-1)$  and  $\text{HCO}^+(1-0)$  are  $-60$  to  $-10\ \text{km s}^{-1}$ ,  $-47$  to  $-20\ \text{km s}^{-1}$  and  $-48$  to  $-26\ \text{km s}^{-1}$ , respectively. For each of the tracers shown as color images the beams are shown in the top left corner of each panel. The radio continuum sources are marked with “+” (white), the ATLASGAL clumps (Csengeri et al. 2014) are marked with filled triangles (black), the  $70\ \mu\text{m}$  bright far-infrared sources are marked with “+” (black) and the  $70\ \mu\text{m}$  dark FIR sources are marked with asterisks. The positional offsets in arcseconds on the two axes are relative to the center ( $\alpha_{2000}$ :  $14^{\text{h}}45^{\text{m}}20.4^{\text{s}}$ ,  $\delta_{2000}$ :  $-59^{\circ}52'03''.5$ ).

diffuse PDR gas. When compared with the  $8\ \mu\text{m}$  Spitzer image the [C II] emission is clearly seen to delineate the rims skirting the bubbles S109 and S111 in particular and matches well with the emission features in the  $8\ \mu\text{m}$  which are due to FUV-excited PAH molecules in the PDRs. The [C II] emission also matches well with the far-infrared dust continuum emission at  $70\ \mu\text{m}$ . The tracers of cold dust ( $870\ \mu\text{m}$  ATLASGAL) and ambient molecular material ( $^{13}\text{CO}(2-1)$  and  $\text{C}^{18}\text{O}(2-1)$ ) primarily show the molecular ridge. The southeastern [C II] peak is detected in both  $^{13}\text{CO}$  and  $\text{C}^{18}\text{O}$ , suggesting a high column density of gas in the region. The  $\text{HCO}^+(1-0)$  map tracing densities in excess of  $10^5\ \text{cm}^{-3}$  shows that this line is detected in the three prominently [C II]-emitting regions, and the emission continues to increase to the north toward the denser part of the molecular ridge. The region hosts a large number of far-infrared sources, some of which are dark even at  $70\ \mu\text{m}$ , and there are quite a few additional cold clumps detected in the  $870\ \mu\text{m}$  ATLASGAL data (marked on Fig.2). The detection of  $\text{HCO}^+(1-0)$  particularly toward the easternmost parts of the northern rim surrounding S111 and the detection of associated far-infrared sources are clear indications of ongoing star formation in dense clumps.

## 5. VELOCITY DISTRIBUTION OF [C II]-EMITTING GAS

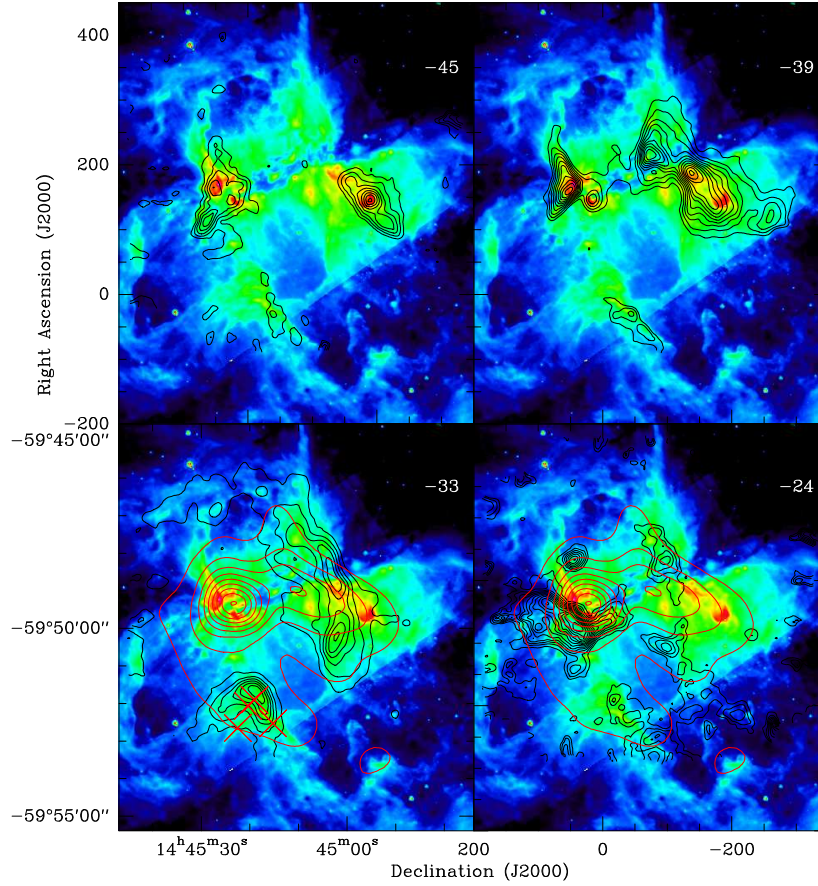


**Figure 3.** Maps of [C II] emission (contours) in  $1 \text{ km s}^{-1}$  wide channels centered at velocities indicated in the panels overplotted on the Spitzer  $8 \mu\text{m}$  continuum image. Contours (red) in the bottom two panels show the 843 MHz radio continuum observed by SUMSS and are drawn from  $0.2$  to  $4.2 \text{ Jy beam}^{-1}$  in steps of  $0.5 \text{ Jy beam}^{-1}$  (for a beam size of  $52'' \times 45''$ ).

### 5.1. Velocity-Channel Maps

Based on velocity-channel maps (Fig. A.1) we identify four distinct velocity ranges of the [C II] emission. Figure 3 compares the [C II] emission in these four velocity ranges centered at  $-45$ ,  $-39$ ,  $-33$  and  $-24 \text{ km s}^{-1}$  with the  $8 \mu\text{m}$  continuum image, which reveals the structure of the region very well. The spatial segregation of emission in the four velocity regions indicates the relative motion primarily of the rims of the bubble S111 and to some extent that of S109. We find that [C II] shows multiple velocity components spanning an interval of  $20 \text{ km s}^{-1}$  spread over about  $300''$ . As detailed later in the paper, these velocity components can be explained by the expansion of the H II region S111.

### 5.2. Position–Velocity Diagrams

A more detailed view of the kinematics of the region can be obtained by studying the position-velocity (p-v) diagrams along a few selected directions. For ease of reference we identify the [C II] prominent emission peaks as clouds A, B, and C (Fig. 4). We considered directions along the ridge (Cut 1), across the S111 bubble (Cut 2) and direction perpendicular to the ridge connecting the [C II] peaks (Cut 3) (Fig. 4). We compare the p-v diagrams of  $^{13}\text{CO}(2-1)$  and [C II] along the three directions. The  $^{13}\text{CO}(2-1)$  emission is representative of the ambient molecular material, while the [C II] mostly represents FUV-irradiated

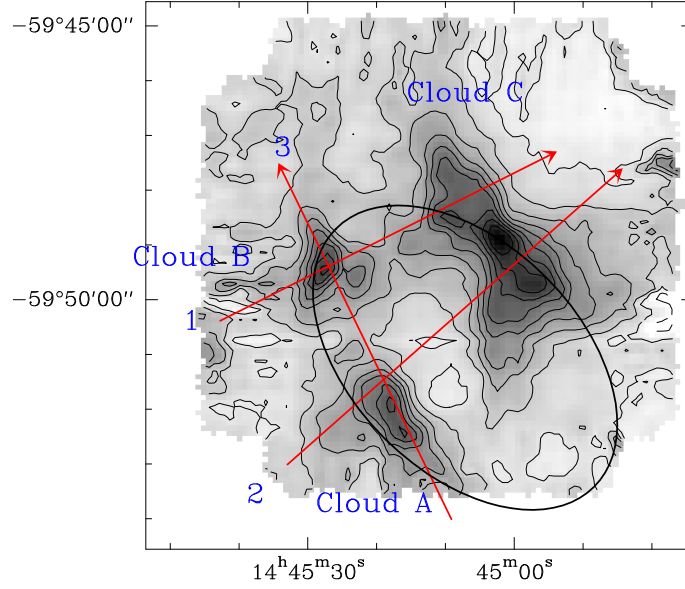


**Figure 4.** Velocity-integrated map of [C II] emission with intensities ranging between 10 and  $540 \text{ km s}^{-1}$  (shown by both color and contours). The contours are separated by  $50 \text{ K km s}^{-1}$ . Straight lines (red) with arrows (marked 1, 2, and 3) show the directions along which position-velocity diagrams shown in Fig. 5 are derived. Clouds A, B, and C discussed in the text are also marked. Also shown is an ellipse approximating the S111 bubble traced by the [C II] contours. The ellipse has semi-major and semi-minor axes of  $200''$  and  $125''$  respectively and a position angle of  $45^\circ$  and is centered at the position with an offset  $-100'', 60''$ .

neutral gas except for the immediate neighborhood of the embedded cluster G316.8-00.05 (Fig. 5). The dotted line in all the p-v diagrams denotes the centroid velocity of the molecular material, supported also by the  $\text{C}^{18}\text{O}(2-1)$  p-v plots (Fig. A.2). Along Cut 1, in the region near the embedded cluster the [C II] emission compares fairly well at velocities around  $-39 \text{ km s}^{-1}$  but shows a distinctly red-shifted component reminiscent of an expanding bubble. The same feature also shows up as isolated red-shifted blobs on the northeastern end of Cut 3. We identify this as the interface of the bubbles S109/S111 that is expanding away from the observer and propose that the expansion is restricted in the opposite direction by the high density molecular material that forms the ridge. Considering the difference in velocities of the molecular material and the PDR gas traced by the [C II], we estimate an expansion velocity of around  $7 \text{ km s}^{-1}$  for part of the rim detected around S111. Along Cut 2 across the bubble S111, the northern [C II] emission feature is faint and compact in velocity in  $^{13}\text{CO}(2-1)$ . However, [C II] at the same position is significantly broadened around the centroid velocity of the ambient medium, possibly due to the presence of young stellar objects (YSOs) that are very bright in the infrared. Along Cut 2, at the inner edge of the bubble S111, the [C II] emission is markedly red-shifted. Along Cut 3, the southwestern clump shows red-shifted emission, while the northeastern clump is somewhat blue-shifted relative to the velocity of the ambient molecular cloud. The velocity distribution seen in the p-v diagrams of [C II] is consistent with emission from FUV-irradiated gas at velocities suggestive of an expanding bubble.

### 5.3. Velocity distribution seen in Azimuthally averaged spectra

The analysis of [C II] emission as a function of velocity in the previous sections of the paper suggests that [C II] traces parts of the expanding bubble S111. The shape of the bubble seen in [C II] is an ellipse with a size of  $400'' \times 250''$  centered at  $\sim -100'', +60''$ , with a position angle of  $45^\circ$  (Fig 4). In order to improve

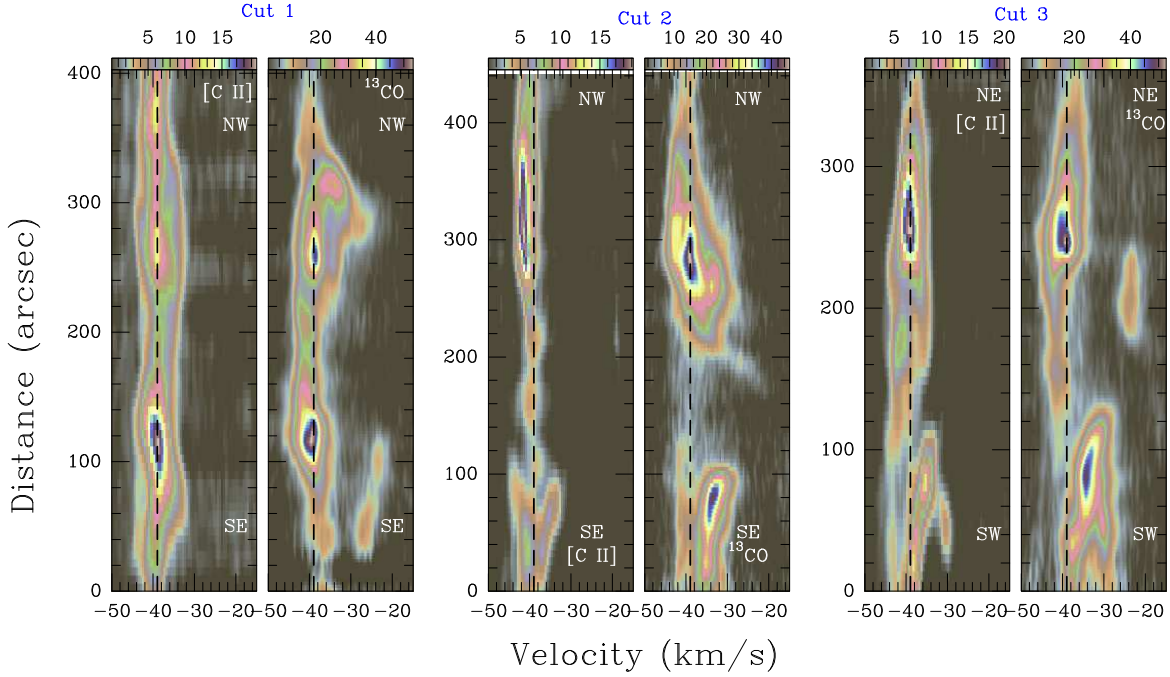


**Figure 5.** Position–velocity maps of  $^{13}\text{CO}(1-0)$  and  $[\text{C II}]$  emission along the Cuts 1, 2, and 3 marked in Fig.4.

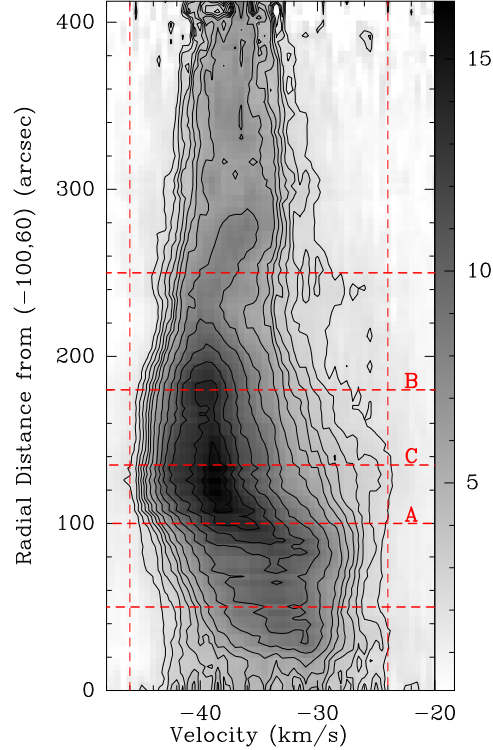


**Figure 6.** Plot of velocity distribution as a function of radial distance from the position  $(-100'', 60'')$ . Each line of the map is the radial profile for one particular plane of the cube and is created by computing annular averages on the data cube. The horizontal dashed lines are drawn at distances of  $50''$ ,  $100''$ ,  $135''$ ,  $180''$ , and  $250''$  from  $(-100'', -60'')$  and show the radial distances of the clouds A, B and C from the same point.

the signal-to-noise ratio of the high-velocity [C II] emission, we have computed the [C II] emission as a function of the radial distance from the assumed center of the bubble, i.e. at an offset  $(-100'', 60'')$  (Fig. 6). Each line of the map is the radial profile for one particular plane of the cube and is created by computing annular averages on the data cube. This plot shows that the [C II] emission is quite broad over the whole nebula, with line widths in the range of  $18 - 22 \text{ km s}^{-1}$  (Fig. 6) consistent with an expanding lobe/bubble with a radius of approximately  $220''$ . The [C II] emission is particularly strong in the interface regions of clouds A, B, and C. There is a clear velocity gradient between clouds A and C, with the bulk of the gas being more redshifted in cloud A than in clouds B and C, likely due to the interaction between the S111 and S109 bubbles. In these radially averaged data the broadest [C II] lines are seen in the direction of cloud C, whereas the p-v plots (Fig. 5) show that the broadest [C II] emission is in the direction of cloud B, which hosts the O-stars responsible for ionizing the H II region. This can be explained by the fact that the cloud C is much more extended in [C II] than cloud B, so that it dominates the radial average of the data, which is more sensitive to the extended emission.

#### 5.4. Analysis of [C II] spectra at selected positions

Figure 7 shows a comparison of [C II],  $^{13}\text{CO}(2-1)$  and  $\text{C}^{18}\text{O}(2-1)$  spectra at selected positions where [C II] emission peaks are observed and which coincide with the locations of Hi-GAL far-infrared sources. The selected positions also sample the environment in the different parts of the arc-shaped rim around S111. The [C II] spectra trace the warm gas around the embedded FIR sources as well as the gas photodissociated by the embedded cluster G316.8-0.05. Therefore the emission profiles appear more complicated than the  $^{13}\text{CO}$  and  $\text{C}^{18}\text{O}$  profiles, which are dominated by the dense molecular gas. Table 1 presents the results of single- or multiple-component Gaussian fits to the [C II],  $^{13}\text{CO}(2-1)$  and  $\text{C}^{18}\text{O}(2-1)$ . We find that the  $\text{C}^{18}\text{O}(2-1)$  profiles are well fitted by a single velocity component although the central velocity appears to vary by more than  $5 \text{ km s}^{-1}$  across the bubble. At all positions, one of the components seen in [C II] matches with the component seen in  $\text{C}^{18}\text{O}$  and with one of the two velocity components typically seen in  $^{13}\text{CO}$ . The larger line widths ( $5-12 \text{ km s}^{-1}$ ) seen in [C II] are likely due to photoevaporative flows of possibly overlapping PDRs. The broad lines seen in  $^{13}\text{CO}(2-1)$  and  $\text{HCO}^+(1-0)$  likely arise from outflows associated with the young embedded far-infrared sources. In particular, the outflow from the embedded YSO is clearly detected in the  $^{13}\text{CO}$  and  $\text{HCO}^+$  spectra of the position with an offset of  $(-20'', 10'')$  which is located in cloud A (Fig. 7).

The [C II] spectra at all positions except toward the center of the star cluster at  $(55'', 155'')$  are more redshifted than the molecular emission. The hydrogen RRLs observed by Longmore et al. (2009) have central velocities between  $-42$  and  $-46 \text{ km s}^{-1}$ , i.e., they are significantly blue-shifted compared to the [C II],  $^{13}\text{CO}$ , and  $\text{C}^{18}\text{O}$  spectra. However, the RRL spectra are much broader than the molecular lines and [C II]. The line widths are between  $20$  and  $24 \text{ km s}^{-1}$ , and therefore they overlap with some of the [C II] spectra. While [C II] may originate from ionized gas as well, in all cases where [C II] is detected at blue-shifted velocities,  $^{13}\text{CO}(2-1)$  is also detected, which implies that the [C II] emission is primarily associated with the neutral gas.

## 6. COLUMN DENSITY AND MASS OF THE [C II]-EMITTING GAS

The velocity distribution of the region with the strongly red-shifted component detected in the [C II] emission does not allow for the detection of the much fainter hyperfine component of  $^{13}\text{C II}$  line, which

**Table 1.** Results of Gaussian fits to spectra

Position (arcsec)	Transition	$v_{\text{LSR}}$ (km s <sup>-1</sup> )	$\Delta v_{\text{LSR}}$ (km s <sup>-1</sup> )	$I$ (K km s <sup>-1</sup> )	$T_{\text{kin}}^a$ (K)
(1)	(2)	(3)	(4)	(5)	(6)
(20, 100)	[C II]	-41.52±0.07	5.07±0.21	59.97±1.89	42
		-36.04±0.14	2.98±0.36	27.21±1.47	
		-23.88±0.15	5.55±0.35	12.70±1.50	
	<sup>13</sup> CO(2-1)	-38.92±0.49	6.90±0.28	25.37±1.42	
		-40.03±0.18	6.77±0.20	66.14±1.55	
	C <sup>18</sup> O(2-1)	-39.40±0.24	6.71±0.43	18.25±1.22	
(55, 155)	[C II]	-39.91±0.25	6.85±0.25	281.08±3.84	90
		-40.11±0.25	3.30±0.25	47.03±3.84	
		-22.55±0.25	5.43±0.25	35.76±3.84	
	<sup>13</sup> CO(2-1)	-38.69±0.5	3.64±0.5	39.88±2.93	
		-39.57±0.5	6.83±0.5	73.22±2.93	
	C <sup>18</sup> O(2-1)	-38.05±0.08	4.40±0.19	31.08±1.08	
(-20, 10)	[C II]	-34.91±0.03	2.38±0.08	47.51±2.39	88
		-33.94±0.03	8.39±0.09	271.40±2.75	
		-35.41±0.04	3.16±0.12	38.82±1.80	
	<sup>13</sup> CO(2-1)	-38.04±0.31	13.75±0.60	48.01±2.47	
		-35.55±0.14	2.96±0.35	8.98±0.88	
	C <sup>18</sup> O(2-1)	-35.55±0.14	2.96±0.35	8.98±0.88	
(-140, 185)	[C II]	-38.98±0.02	3.63±0.08	144.18±6.36	93
		-34.71±0.09	8.02±0.13	297.54±6.69	
		-42.64±0.02	2.67±0.05	67.73±1.43	
	<sup>13</sup> CO(2-1)	-36.31±0.21	4.55±0.48	17.98±1.83	
		-40.70±0.03	3.22±0.07	69.32±1.71	
	C <sup>18</sup> O(2-1)	-40.71±0.06	2.11±0.15	10.15±0.59	
(-130, 85)	[C II]	-34.09±0.25	4.37±0.25	8.03±2.56	69
		-34.03±0.25	9.22±0.25	195.84±2.56	
		-32.59±0.25	3.34±0.25	41.51±2.56	
	<sup>13</sup> CO(2-1)	-32.51±0.06	3.28±0.13	26.00±0.92	
		-39.55±0.13	4.72±0.39	21.04±1.19	
	C <sup>18</sup> O(2-1)	-32.58±0.18	2.50±0.37	5.25±0.71	

NOTE—<sup>a</sup> Planck-corrected peak temperature of the [C II] spectrum assumed to be optically thick.

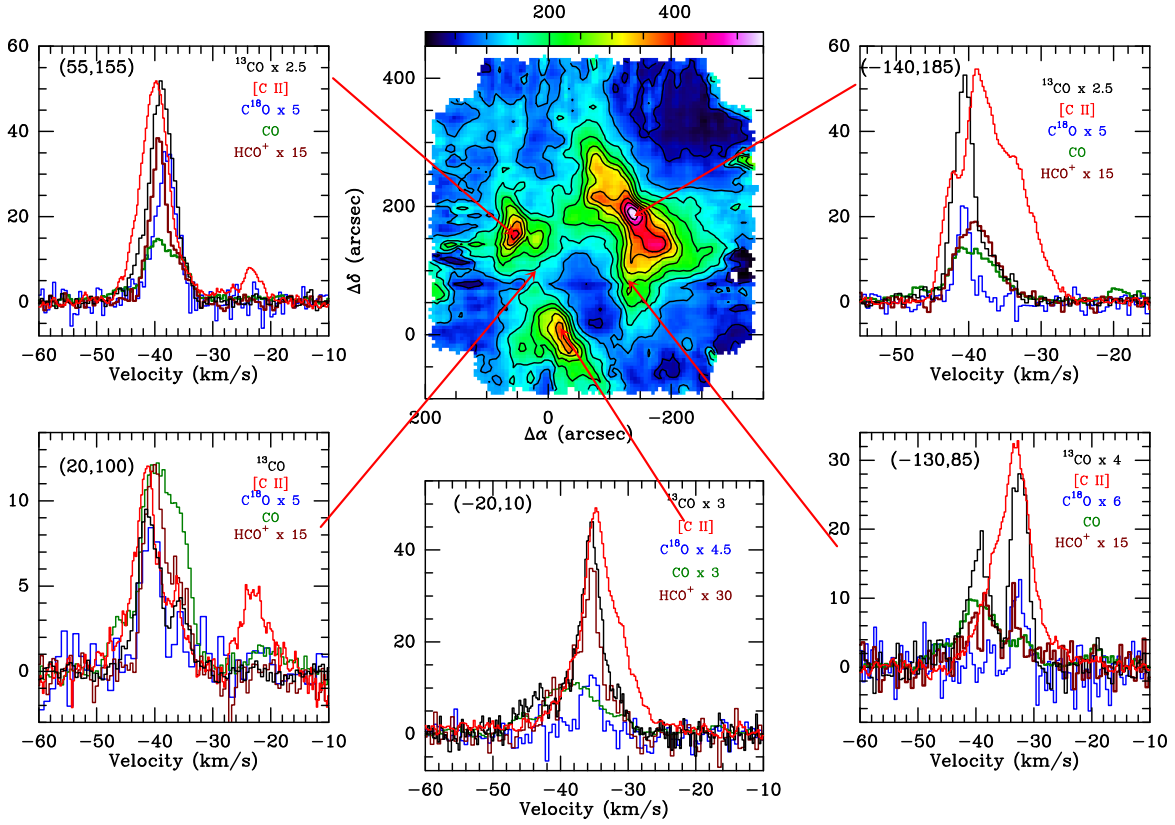


**Figure 7.** Comparison of spectra at selected positions in the observed [C II] map (shown in the middle). In each panel the offset of the position relative to ( $\alpha_{2000}$ :  $14^{\text{h}}45^{\text{m}}20.4^{\text{s}}$ ,  $\delta_{2000}$ :  $-59^{\circ}52'03''.5$ ) is marked and [C II] (black), CO(1–0) (purple),  $^{13}\text{CO}(2-1)$  (red),  $\text{C}^{18}\text{O}(2-1)$  (blue), and  $\text{HCO}^+(1-0)$  (brown) spectra are shown. Single- or multiple-component Gaussian fits to the three spectra at each position were performed and the results are shown as green continuous curves with details presented in Table 1. The spectra are scaled by the factors mentioned in the panels for better visibility.

lies at  $v = +11 \text{ km s}^{-1}$  relative to the [C II] line. However, in recent velocity-resolved observations, the [C II] emission from most Galactic PDRs has been found to be optically thick (Mookerjea et al. 2021; Guevara et al. 2020; Mookerjea et al. 2019). The PDR gas in the G316.75 region being studied here is reasonably bright and high-density clumps are seen in the [C II] emission as well. We thus consider the [C II] emission to be optically thick and use the Rayleigh-Jeans corrected peak brightness temperature of [C II] spectra as an estimate of the kinetic temperature of the PDR gas (Column 6 of Table 1) and also for the estimation of  $N(\text{C}^+)$  from the observed velocity-integrated [C II] intensity. We first consider the contribution of ionized gas close to the H II region. Comparison of the [C II] emission with the  $\text{H}57\alpha$  (Longmore et al. 2009) emission map suggests that the peak of the [C II] emission is shifted by about  $10''$ , which is within the  $14''$  beam of the [C II] data. Watkins et al. (2019) explained the small ionized gas fraction in the ridge G316.75 as a consequence of the large electron ( $n_e=5000 \text{ cm}^{-3}$ ) and  $\text{H}_2$  gas densities in the immediate vicinity of the ionizing high-mass stars. If we assume  $n_e=5000 \text{ cm}^{-3}$  and follow the formulation presented by Pabst et al. (2017, Equation 7) to estimate the contribution of the ionized gas to the [C II] intensities close to the H II region we obtain an integrated [C II] intensity of  $497 \text{ K km s}^{-1}$ . The [C II] intensity estimated to arise from the ionized gas is therefore comparable to the peak [C II] intensity of  $437 \text{ K km s}^{-1}$  found at this position. However, unlike the prediction of the model constructed

by [Watkins et al. \(2019\)](#), the H57 $\alpha$  emission suggests that such high-density ionized gas to be confined to within 30'' of the peak of ionized emission. At the other extreme ( $n_e \sim 60 \text{ cm}^{-3}$ ) of the range of electron densities proposed by [Watkins et al.](#), the [C II] emission would be only 6 K km s $^{-1}$ , far less than the faintest level (180 K km s $^{-1}$ ) level of [C II] emission in the immediate vicinity of the H II region (Fig. 4). Thus, we conclude that while for the peak position of the H II region there is a significant contribution of the ionized gas to the [C II] emission, the more extended emission is dominated by the neutral PDR gas.

In the neutral region, where C $^+$ -H and C $^+$ -H $_2$  collisions dominate, we estimate  $N(\text{C}^+)$  (in cm $^{-2}$ ) from the observed integrated [C II] intensities using Eq. (26) from [Goldsmith et al. \(2012\)](#) as follows:

$$N(\text{C}^+) = 2.91 \times 10^{15} \left[ 1 + 0.5e^{91.25/T_{\text{kin}}} \left( 1 + \frac{A_{\text{ul}}}{C_{\text{ul}}} \right) \right] \int T_{\text{mb}} dv \quad (1)$$

where  $A_{\text{ul}} = 2.3 \times 10^{-6} \text{ s}^{-1}$ ,  $T_{\text{kin}}$  is the gas kinetic temperature, the collision rate is  $C_{\text{ul}} = R_{\text{ul}}n$  with  $R_{\text{ul}}$  being the collision rate coefficient with H $_2$  or H $^0$ , which depends on  $T_{\text{kin}}$ , and  $n$  is the volume density of H. At  $T_{\text{kin}} = 100 \text{ K}$  for C $^+$ -H collisions  $R_{\text{ul}} = 7.6 \times 10^{-10} \text{ cm}^3 \text{ s}^{-1}$  and  $R_{\text{ul}} = 3.8 \times 10^{-10} \text{ cm}^3 \text{ s}^{-1}$  for C $^+$ -H $_2$  collisions. Since the critical density of the [C II] transition is  $n_{\text{cr}} = 3000 \text{ cm}^{-3}$ , and since it is likely that most of the [C II] detected could be at such densities along with some emission arising from clumps with densities exceeding  $10^5 \text{ cm}^{-3}$ , we assume a density of  $10^4 \text{ cm}^{-3}$  to estimate the  $N(\text{C}^+)$  density distribution of the region. Assuming a kinetic temperature of 100 K for C $^+$  and a density of  $n = 10^4 \text{ cm}^{-3}$ , and excitation from C $^+$ -H $_2$  collisions, the column density is found to lie in the range  $(0.7-4.5) \times 10^{18} \text{ cm}^{-2}$ . A combination of slightly different  $T_{\text{kin}}$  and density and the inclusion of C $^+$ -H collisions would result in an uncertainty of no more than 30% in the column density. Based on the values of  $A_{\text{ul}} = 2.3 \times 10^{-6} \text{ s}^{-1}$  and  $n_{\text{cr}}$  at 100 K and C/H =  $3 \times 10^{-4}$ , the [C II] line is expected to be optically thick for  $N(\text{C}^+) = 4 \times 10^{17} \text{ cm}^{-2}$  (Table 2.7 in [Tielens 2005](#)). The estimated values of  $N(\text{C}^+)$  thus validate our assumption of the [C II] line being optically thick.

We estimate the mass of the [C II]-emitting gas, which is dominated by the three regions named clouds A, B and C (Fig. 4). For the observed [C II] intensities, a distance of 2.7 kpc and a C/H abundance ratio of  $1.3 \times 10^{-4}$  of which approximately 50% of carbon resides in C $^+$ , we find the total molecular H $_2$  masses of clouds A, B and C to be 1000, 640, and 2500  $M_{\odot}$  respectively. We have also estimated the mass of the molecular gas in clouds A, B, and C using the  $N(\text{H}_2)$  maps derived by [Samal et al. \(2018\)](#) based on Herschel observations. We find the H $_2$  mass estimated from dust continuum observations in clouds A, B, and C to be 2000, 3400, and 5000  $M_{\odot}$  respectively. The estimate of the total molecular gas mass within the lowest [C II] contour shown in Fig 4 is 6900  $M_{\odot}$  from [C II] data and 18,100  $M_{\odot}$  from the dust continuum. Thus, we see that in clouds A and C, which are bright in far-infrared dust continuum as well as [C II], about 50% of the mass is traced by the [C II] emission, whereas in cloud B, in which the ionizing stars reside, only 18% of the mass is traced by [C II]. The lower fraction of molecular mass being traced by [C II] in this region is likely due to the high densities in the ridge, which shields it from the FUV radiation, unlike the rest of the cloud. The [C II] emission seen from the ridge is likely due to dense the ionized gas near the center of the H II region and diffuse PDR further out. This indication of higher density material to the north along the ridge is corroborated by the analysis presented by [Watkins et al. \(2019\)](#) in support of the lower than expected effect of the embedded cluster on the ridge itself. We propose that the bipolar H II region clears off part of the bubble, and the FUV radiation leaking through the bubble creates PDRs on the surface of the G316.75 ridge.

## 7. ESTIMATE OF MECHANICAL FEEDBACK FROM THE STARS ON S111

### 7.1. Energy budget in S111

The triple bubble system of S109, S110 and S111 has putatively been created by the massive stellar cluster embedded in the G316.75 ridge. While the three bubbles are connected through their history of formation, in the present configuration the H II regions appear to be segregated by the dense ridges or shells of swept-up gas and hence can be studied in isolation. Our study focuses on the mechanical and radiative feedback from the embedded stars.

We first estimate the role of mechanical feedback from the ionizing stars by comparing the kinetic energy of the shell to the thermal energy of the ionized gas in S111. The [C II] observations suggest that the denser parts of the clouds A and C represent part of the shell created by the expanding H II region. These have velocities red-shifted by about  $5\text{--}6\text{ km s}^{-1}$  relative to cloud B, which hosts the ionizing stars (Table 1, Fig. 5). Additionally more diffuse PDR material also traced by [C II] are red-shifted by  $15\text{ km s}^{-1}$  at the boundary between the bubbles S109 and S111. Thus, the shells of S111 appear to move at relatively slow speeds, particularly when contrasted with the shells that have been observed in Orion, RCW 120, and RCW 49 (Pabst et al. 2020; Luisi et al. 2021; Tiwari et al. 2021). The high-density material toward the northern part of the ridge seen in the molecular line observations most likely contributes to the slowing down of the expansion of the H II region and the shell. We estimate the kinetic energy of the clouds A and C with a mass of  $7000 M_{\odot}$  moving with a velocity of  $7\text{ km s}^{-1}$  relative to B to be  $3.4 \times 10^{48}\text{ erg}$ .

The H II region S111 has a radius of  $\sim 160''$  (2 pc at a distance of 2.7 kpc) (Fig. 4) and Watkins et al. (2019) estimated a temperature  $T_{\text{HII}} = 6600\text{ K}$  and density  $n_e = 60\text{--}5000\text{ cm}^{-3}$ . The total thermal energy of the S111 H II region can be written as  $E_{\text{th}} = \frac{3}{2} n_e \frac{4\pi}{3} R^3 k_B T_{\text{HII}}$ , where  $R$  is the radius of the H II region and  $k_B$  is the Boltzmann constant. We estimate the  $E_{\text{th}}$  to range between  $8.1 \times 10^{46}$  and  $6.7 \times 10^{48}\text{ erg}$  for  $n_e = 60$  and  $5000\text{ cm}^{-3}$  respectively.

Thus, depending on the actual electron density of the H II region, the kinetic energy of the molecular shells primarily detected in [C II] is between  $\sim 0.5\text{--}40$  times the thermal energy of the H II region.

### 7.2. Pressure balance of S111

The impact of high-mass stars on the ambient molecular cloud can be further quantified in terms of the pressures associated with direct radiation ( $P_{\text{dir}}$ ), dust-processed radiation ( $P_{\text{IR}}$ ), photoionization heating ( $P_{\text{ion}}$ ) and shock heating from stellar winds ( $P_X$ ). No X-ray mapping observations are available for the H II region associated with S111, hence  $P_X$  could not be estimated. Thus, we next consider the pressures associated with the other feedback mechanisms from the high-mass stars in the neighborhood of S111.

The pressure due to the photoionization heating of the gas in the region,  $P_{\text{ionized}}/k_B = n_e T_{\text{HII}}$  is estimated to be between  $(0.4\text{--}33) \times 10^6\text{ K cm}^{-3}$  for electron densities of  $60\text{--}5000\text{ cm}^{-3}$  respectively.

Following Olivier et al. (2021), we define the direct radiation pressure ( $P_{\text{dir}}$ ) as the momentum available to drive motion in the shells in the H II region at a radius  $R$  from the central stars (Eq. 3)

$$P_{\text{dir}} = \frac{3L_{\text{bol}}}{4\pi R^2 c}, \quad (2)$$

where  $L_{\text{bol}}$  is the bolometric luminosity of central stars. The total bolometric luminosity of the two central ionizing stars, one O7V and the other O6V, is  $3.5 \times 10^5 L_{\odot}$  and the total production rate of ionizing photons is  $1.56 \times 10^{49}\text{ s}^{-1}$ . The direct pressure ( $P_{\text{dir}}/k_B$ ) at the location of the inner edge of the shell located at a radius of  $160''$  (2 pc) from the stellar cluster is therefore  $9.3 \times 10^5\text{ K cm}^{-3}$ .

In another feedback mode, stellar radiation is absorbed by dust and thermally reradiated in the IR wavelengths, and this induces a dust-processed radiation pressure that is given by (Eq. 2 in Olivier et al. 2021)

$$P_{\text{IR}} = \frac{1}{3V} a T_d^4 \frac{4\pi}{3} (R_{\text{shell}}^3 - R^3), \quad (3)$$

where  $R_{\text{shell}}$  is the outer radius of the shell,  $R$  is the inner radius of the shell, which is the same as the radius of the H II region, and  $V$  is the volume of the H II region. Based on the dust temperatures  $T_d$  derived by Samal et al. (2018), we assume the dust temperature in the shell to be around 24 K. From the position-velocity plots (Fig 5) we estimate the thickness of the shell to be  $20''$  (0.3 pc), resulting in a dust-processed radiation pressure  $P_{\text{IR}}/k_B$  of  $6 \times 10^6 \text{ K km s}^{-1}$ .

Finally, we estimate the thermal pressure ( $P_{\text{PDR}}$ ) of [C II]-emitting PDR gas. We assume the hydrogen volume density of the PDR to be  $n_{\text{H}} = 3 \times 10^3 \text{ cm}^{-3}$ , which is the critical density ( $n_{\text{cr}}$ ) for the [C II] transition, and the gas temperature ( $T_{\text{PDR}}$ ) to be 100 K based on our estimates in Section 6. Thus  $P_{\text{PDR}} = n_{\text{H}} k_B T_{\text{PDR}} = 3 \times 10^5 \text{ K km s}^{-1}$ . It is likely that the value of  $P_{\text{PDR}}$  is an underestimate, since we have considered only the diffuse component of the PDR and it could easily be a factor of three larger, in which case it would be comparable to  $P_{\text{dir}}$ .

We find that among all factors contributing to pressure,  $P_{\text{ion}}$  is the most important, and depending on the electron density it is of similar in magnitude to  $P_{\text{IR}}$  of the shell around the H II region. In this analysis, we have not considered the dust-processed radiation pressure inside the H II region since there is very faint or almost no dust continuum detected from within the H II region even in the SPIRE 250  $\mu\text{m}$  maps. We find that  $P_{\text{dir}}$  and  $P_{\text{PDR}}$  are lower than  $P_{\text{IR}}$  by factors of 6 and 20, respectively. Olivier et al. (2021) considered resolved compact H II regions and found that most of the sources are dominated by  $P_{\text{IR}}$ , and the median  $P_{\text{dir}}$  and  $P_{\text{ion}}$  are smaller than the median  $P_{\text{IR}}$  by factors of 6 and 9 respectively. Based on the radial dependence of pressure terms, these authors concluded that the H II regions transition from  $P_{\text{IR}}$ -dominated to  $P_{\text{ion}}$ -dominated at radii of  $\sim 3 \text{ pc}$ . Our conclusions for the S111 H II region, which has a radius of about 2 pc with a shell of about 0.3 pc thickness, are consistent with the results obtained by Olivier et al. (2021).

## 8. DISCUSSION

The velocity-resolved observations of [C II] have enabled a tomographic study of the expanding shell associated with the bubble S111 formed by the embedded cluster G316.8-00.05. The expansion of the bubble at  $\sim 7 \text{ km s}^{-1}$  is primarily observed in the red-shifted velocities with no blue-shifted counterparts. This suggests that the bubble is able to expand more freely in a direction away from the observer, possibly due to the presence of higher density material between the rim of S111 and the observer. The H II region associated with S111 plays a key role in providing the pressure for the expansion of the shell in the ambient molecular medium. We estimate ionization of hydrogen ( $P_{\text{ion}}$ ) and dust-reprocessed radiation ( $P_{\text{IR}}$ ) to be the primary contributors to the pressures in the region. We find that the kinetic energy of part of the molecular shell associated with clouds A and C is 0.5–40 times the total thermal energy of the H II region. We do not see any evidence of injection of energy by stellar winds from the massive stars; the moderate expansion velocity of the shell can be well explained by the smooth expansion of the H II region. This is in contrast to several recent studies of the feedback of massive stars on their environment, which imply a significant role of the stellar winds in the Orion veil shell, RCW 120, and RCW 49 (Pabst et al. 2020; Luisi et al. 2021; Tiwari et al. 2021). There is a distinct difference between the ionizing stars in the G316.75 region and regions studied by the above-mentioned works. The ionizing stars in Orion, RCW 120, and RCW 49 have already cleared the surrounding region, whereas the G316.80-0.05 cluster is still deeply embedded in dense

molecular material with a line-of-sight visual extinction exceeding 100 mag. This suggests that the impact of the stellar winds, if any, from G316.8-0.05 could have also been contained within a very small region due to the high densities of the region.

The dense rim created by the expansion of the bubble has been studied in terms of the three clouds A, B, and C, with cloud B being coincident with the ridge G316.75, which is dark in the mid-infrared and hosts the massive stellar cluster that gave rise to the triple bubble system. Clouds A and C are created by the compression of molecular material by the expanding bubble and contain embedded far-infrared sources that are indicative of formation of a new generation of stars. The two [C II] emission peaks in cloud B are associated with far-infrared sources detected at  $\lambda > 70 \mu\text{m}$  as well as with  $870 \mu\text{m}$  ATLASGAL sources. The [C II] peak in the cloud C coincides with the ATLASGAL source G316.768-00.026, which remains undetected at  $\lambda < 160 \mu\text{m}$ , consistent with a YSO at a very early stage of evolution. Most of the YSOs identified based on mid-infrared colors (Samal et al. 2018) lie along the northern part of the region, with one lying very close to the head of cloud A, one close to cloud B, and two in cloud C. One of the reasons for the nondetection of YSOs in the region is attributed to the high degree of obscuration along this line of sight.

Cloud A in particular appears to have a structure similar to the pillars created by the UV erosion of molecular material (Fig. 3). At the head of cloud A ( $-20'', 10''$ ) an outflow is detected in the form of a pronounced blue wing in the  $^{13}\text{CO}(2-1)$  and  $\text{HCO}^+(1-0)$  spectra (Fig. 7) arising from the embedded YSO. The outflow coincides with the ATLASGAL source G316.778-00.096, which is also detected in the far-infrared Hi-GAL images with its intensities peaking at  $160 \mu\text{m}$ . Elia et al. (2017) have identified this source as HIGALBM 316.7799-0.0942 and have derived a mass of  $234.6 M_{\odot}$ , a bolometric luminosity of  $1187 L_{\odot}$ , and a bolometric temperature of  $38.6 \text{ K}$ . While no other signs of star formation have yet been reported, the detection of broad spectra consistent with an outflow, high densities (based on detection of  $\text{HCO}^+(1-0)$ ) along with the presence of a compact far-infrared source are clearly indicative of ongoing star formation activity. Based on the mass estimated for the continuum source and the distance to the region, it is possible that a star cluster is being formed at the head of cloud A. The H II region of S111 is estimated to have an age of 2 Myr, which when compared with typical formation timescales of high-mass stars implies that the star formation activity in cloud A is more recent and hence likely triggered by the expansion of S111.

## 9. CONCLUSIONS

We have used velocity-resolved observations of the  $^2\text{P}_{3/2} \rightarrow ^2\text{P}_{1/2}$  transition of [C II] and the  $J=2-1$  transition of  $^{13}\text{CO}$  and  $\text{C}^{18}\text{O}$  to study the infrared bubble S111, which lies in the region surrounding the southern part of the infrared dark ridge G316.75. The [C II] emission from the region primarily arises from the shells irradiated by the embedded cluster G316.80-0.05, part of this photodissociated gas in the shell in cloud C not being detected in  $^{13}\text{CO}(2-1)$  and  $\text{C}^{18}\text{O}(2-1)$ . In the dense ridge G316.75 the [C II] emission arises due to photodissociation of the molecular material by the stellar radiation leaking out into the bubble and not through the dense ridge. The [C II] emission traces the low-density PDR gas and shows dense clumps that emit  $\text{HCO}^+(1-0)$  as well. However, in the absence of any other PDR tracer it is not possible to further constrain the properties of the PDR gas.

The velocity information of the [C II] data in particular enabled us to decipher the morphology of the expanding shell and evaluate the feedback from the massive star cluster on the surrounding ISM. The expanding shell is primarily propelled by the H II region created by the embedded cluster G316.8-0.05. Azimuthally averaged [C II] data were used to conclusively show that the entire velocity structure seen in [C II] can be explained by layers of a single shell expanding with a moderate velocity of  $\sim 7 \text{ km s}^{-1}$  around

S111. We conclude that the kinetic energy of the expanding part of the shell is comparable to or larger than the thermal energy of the H II region. We have also quantified the contribution of the stellar radiation to the pressure in the region and conclude that the thermal pressure of the H II region and the dust-processed radiation pressure are the most significant components. We present here a clear evidence of star formation triggered by the compression of the ISM due to the expanding bubble S111.

The author acknowledges the insightful discussions with Dr G. Sandell during the writing of the manuscript. This work was supported by funding by the Department of Atomic Energy, Government of India, under Project Identification No. RTI 4002. Based on observations made with the NASA/DLR Stratospheric Observatory for Infrared Astronomy (SOFIA). SOFIA is jointly operated by the Universities Space Research Association, Inc. (USRA), under NASA contract NAS2-97001, and the Deutsches SOFIA Institut (DSI) under DLR contract 50 OK 0901 to the University of Stuttgart. The development of GREAT was financed by the participating institutes, by the Federal Ministry of Economics and Technology via the German Space Agency (DLR) under Grants 50 OK 1102, 50 OK 1103 and 50 OK 1104 and within the Collaborative Research Centre 956, sub-projects D2 and D3, funded by the Deutsche Forschungsgemeinschaft (DFG). This research has made use of the Vizier catalog access tool, CDS, Strasbourg, France. The original description of the Vizier service was published in *A&AS* 143, 23. The ATLASGAL project is a collaboration between the Max-Planck-Gesellschaft, the European Southern Observatory (ESO) and the Universidad de Chile. It includes projects E-181.C-0885, E-078.F-9040(A), M-079.C-9501(A), M-081.C-9501(A) plus Chilean data. This paper made use of information from the SEDIGISM survey database located at <https://sedigism.mpifr-bonn.mpg.de/index.html>, which was constructed by James Urquhart and hosted by the Max Planck Institute for Radio Astronomy.

## REFERENCES

- Churchwell, E., Povich, M. S., Allen, D., et al. 2006, *ApJ*, 649, 759
- Csengeri, T., Urquhart, J. S., Schuller, F., et al. 2014, *A&A*, 565, A75
- Dalglish, H. S., Longmore, S. N., Peters, T., et al. 2018, *MNRAS*, 478, 3530
- Deharveng, L., Schuller, F., Anderson, L. D., et al. 2010, *A&A*, 523, A6
- Elia, D., Molinari, S., Schisano, E., et al. 2017, *MNRAS*, 471, 100
- Foster, J. B., Jackson, J. M., Barnes, P. J., et al. 2011, *ApJS*, 197, 25
- Foster, J. B., Rathborne, J. M., Sanhueza, P., et al. 2013, *PASA*, 30, e038
- Goldsmith, P. F., Langer, W. D., Pineda, J. L., & Velusamy, T. 2012, *ApJS*, 203, 13
- Guevara, C., Stutzki, J., Ossenkopf-Okada, V., et al. 2020, *A&A*, 636, A16
- Hanaoka, M., Kaneda, H., Suzuki, T., et al. 2020, *PASJ*, 72, 5
- Heyminck, S., Graf, U. U., Güsten, R., et al. 2012, *A&A*, 542, L1
- Jackson, J. M., Rathborne, J. M., Foster, J. B., et al. 2013, *PASA*, 30, e057
- Krumholz, M. R., Burkhart, B., Forbes, J. C., & Crocker, R. M. 2018, *MNRAS*, 477, 2716
- Longmore, S. N., Burton, M. G., Keto, E., Kurtz, S., & Walsh, A. J. 2009, *MNRAS*, 399, 861
- Luisi, M., Anderson, L. D., Schneider, N., et al. 2021, *Science Advances*, 7, eabe9511
- Mauch, T., Murphy, T., Buttery, H. J., et al. 2003, *MNRAS*, 342, 1117
- Molinari, S., Swinyard, B., Bally, J., et al. 2010, *A&A*, 518, L100
- Mookerjea, B., Sandell, G., Güsten, R., et al. 2019, *A&A*, 626, A131
- Mookerjea, B., Sandell, G., Veena, V. S., et al. 2021, *A&A*, 648, A40
- Olivier, G. M., Lopez, L. A., Rosen, A. L., et al. 2021, *ApJ*, 908, 68

- Pabst, C. H. M., Goicoechea, J. R., Teyssier, D., et al. 2017, *A&A*, 606, A29
- . 2020, *A&A*, 639, A2
- Peretto, N., & Fuller, G. A. 2009, *A&A*, 505, 405
- Samal, M. R., Deharveng, L., Zavagno, A., et al. 2018, *A&A*, 617, A67
- Schuller, F., Urquhart, J. S., Csengeri, T., et al. 2021, *MNRAS*, 500, 3064
- Shaver, P. A., Retallack, D. S., Wamsteker, W., & Danks, A. C. 1981, *A&A*, 102, 225
- Tielens, A. G. G. M. 2005, *The Physics and Chemistry of the Interstellar Medium* (Cambridge University Press)
- Tiwari, M., Karim, R., Pound, M. W., et al. 2021, *ApJ*, 914, 117
- Vig, S., Ghosh, S. K., Ojha, D. K., & Verma, R. P. 2007, *A&A*, 463, 175
- Watkins, E. J., Peretto, N., Marsh, K., & Fuller, G. A. 2019, *A&A*, 628, A21
- Young, E. T., Becklin, E. E., Marcum, P. M., et al. 2012, *ApJL*, 749, L17

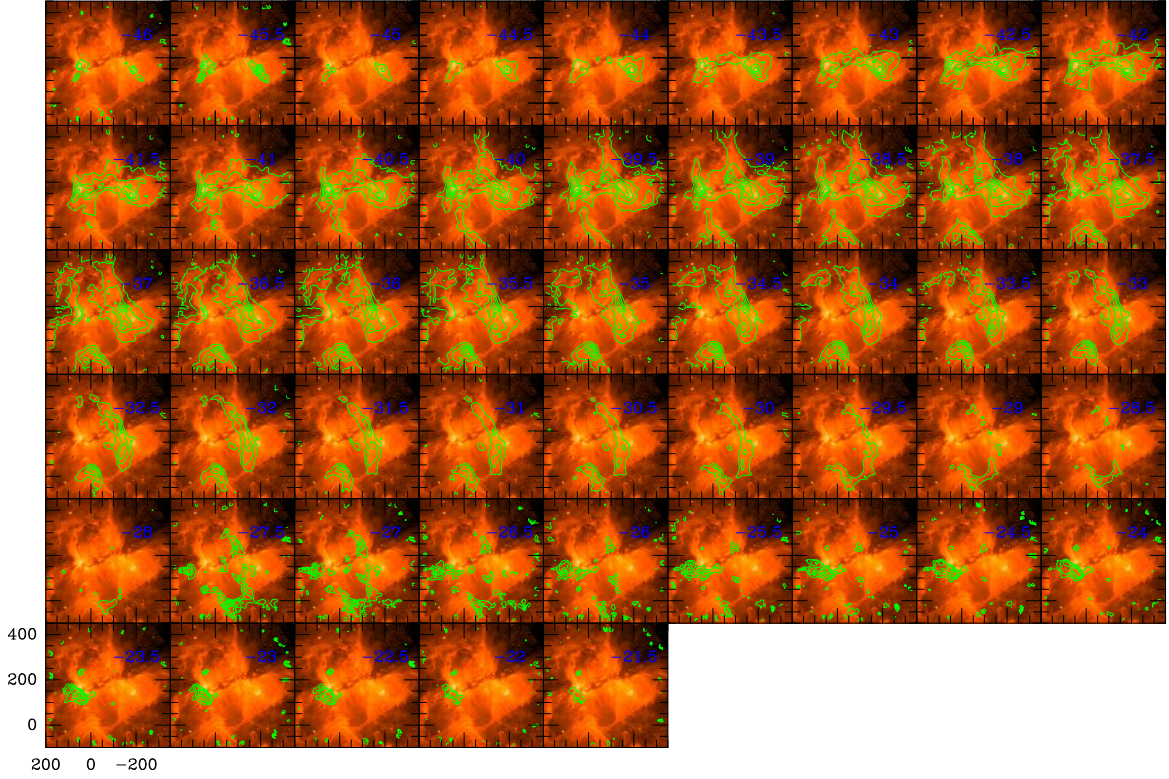


**Figure A.1.** Channel maps of [C II] emission (contours) overlaid on Spitzer  $8\mu\text{m}$  continuum image (color). The positional offsets are relative to the center ( $\alpha_{2000}$ :  $14^{\text{h}}45^{\text{m}}20.4^{\text{s}}$ ,  $\delta_{2000}$ :  $-59^{\circ}52'03''.5$ ).

## APPENDIX

### A. ADDITIONAL FIGURES

Figure A.1 presents the channel maps of [C II] emission discussed in Section 5.1. Figure A.2 shows the position-velocity diagrams for  $\text{C}^{18}\text{O}(2-1)$  which are discussed in Section 5.2.

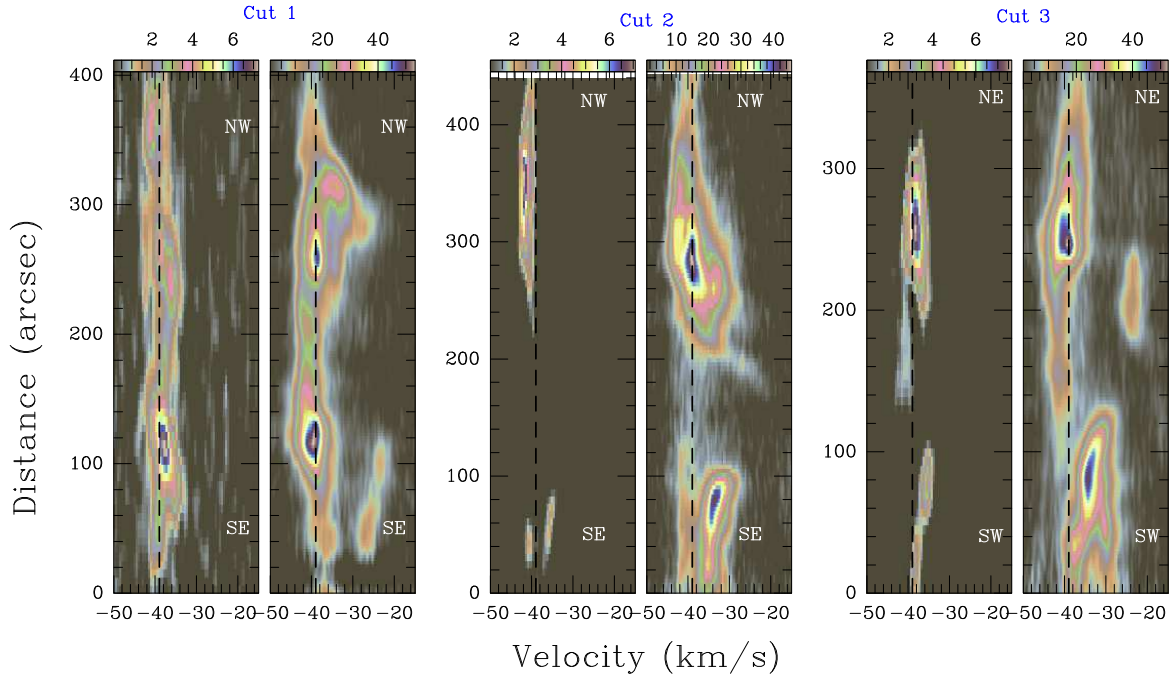


**Figure A.2.** Position-velocity maps of  $\text{C}^{18}\text{O}(1-0)$  and  $[\text{C II}]$  emission along the Cuts 1, 2 and 3 marked in Fig.4.